Viewing Geometry Dependencies in MODIS Cloud Products

B. C. MADDUX AND S. A. ACKERMAN

Department of Atmospheric and Oceanic Sciences, and Cooperative Institute for Meteorological Satellite Studies, University of Wisconsin—Madison, Madison, Wisconsin

S. PLATNICK

Laboratory for Atmospheres, NASA Goddard Space Flight Center, Greenbelt, Maryland

(Manuscript received 11 December 2009, in final form 6 April 2010)

ABSTRACT

Characterizing the earth's global cloud field is important for the proper assessment of the global radiation budget and hydrologic cycle. This characterization can only be achieved with satellite measurements. For complete daily coverage across the globe, polar-orbiting satellites must take observations over a wide range of sensor zenith angles. This paper uses Moderate Resolution Imaging Spectroradiometer (MODIS) Level-3 data to determine the effect that sensor zenith angle has on global cloud properties including the cloud fraction, cloud-top pressure, effective radii, and optical thickness. For example, the MODIS cloud amount increases from 57% to 71% between nadir and edge-of-scan (~67°) observations, for clouds observed between 35°N and 35°S latitude. These increases are due to a combination of factors, including larger pixel size and longer observation pathlength at more oblique sensor zenith angles. The differences caused by sensor zenith angle bias in cloud properties are not readily apparent in monthly mean regional or global maps because the averaging of multiple satellite overpasses together "washes out" the zenith angle artifact. Furthermore, these differences are not constant globally and are dependent on the cloud type being observed.

1. Introduction

The global cloud field is highly variable in both space and time. Assessing when and where clouds occur, and their higher-order properties, is key to understanding the role clouds play in the earth's radiation budget and hydrological cycle. Only observations from satellite platforms provide the needed global coverage at a temporal resolution high enough for this assessment. Retrieval of cloud properties has been made using a variety of methods and satellite instruments (e.g., Rossow 1989; Twomey and Cocks 1989; Nakajima and King 1990; Platnick and Twomey 1994; Rossow and Schiffer 1999; Wylie and Menzel 1999; Platnick et al. 2003; Heidinger 2003; Minnis 1989; Ackerman et al. 1998; Frey et al. 2008; Wylie et al. 2007). Preliminary comparisons of available climatological satellite datasets, using the most basic of cloud descriptors such as cloud fractional coverage, yield differences that can exceed the mean global annual cycle within each dataset (Thomas et al. 2004; Stubenrauch et al. 2006; Stubenrauch and Kinne 2009).

Significant effort has been given to characterizing the uncertainties and sensitivities of various global cloud climatologies using independent measurements from ground, aircraft, and, more recently, satellite platforms (e.g., Holz et al. 2008; Ackerman et al. 2008; Kahn et al. 2007; Mahesh et al. 2004; Malberg 1973; Min et al. 2004; Zhao and Girolamo 2006; Naud et al. 2004; Mace et al. 2005; Smith and Platt 1978). The more fundamental differences leading to discrepancies in the comparisons include instrument capabilities (spectral coverage, spatial resolution, and swath), retrieval algorithms, and the spatiotemporal sampling available from the satellite orbit. Attributing differences to either natural or artificial causes is key to understanding and interpreting satellite data records. The effects of satellite-observing angle characteristics have been discussed as one such artifact (e.g., Minnis 1989; Zhao and Di Girolamo 2004; Tan et al. 2006; Ackerman et al. 2008).

The dependencies of cloud properties on viewing geometry are undesirable but unavoidable when using satellite data. Instruments on both geostationary and

Corresponding author address: Brent C. Maddux, 1225 West Dayton St., Madison, WI 53706.
E-mail: brentm@ssec.wisc.edu

DOI: 10.1175/2010JTECHA1432.1

© 2010 American Meteorological Society

polar- orbiting satellites take observations across a breadth of solar scattering angles and sensor zenith angles, each with its own viewing geometry characteristics. This paper quantifies the effects of the sensor zenith angle dependence on the Level-3 cloud properties derived from Moderate Resolution Imaging Spectroradiometer (MODIS) observations.

2. Data

This study uses the daily Level-3 *Aqua* and *Terra* MODIS Collection-5 datasets for the complete years of 2003–2007 (King et al. 2003; Frey et al. 2008). *Terra* was launched on 18 December 1999, with data available from 24 February 2000 to present. *Aqua* was launched on 4 May 2002, becoming the first member of the Afternoon Constellation (or A-train), with MODIS opening its shutter on 4 July 2002 and data available to the present. The *Terra* and *Aqua* daytime equatorial crossing times are 1030 and 1330 LT, respectively. The orbits have remained extremely stable in both space and time. For example, the *Aqua* mission requirement was for a 1330 to 1345 LT equatorial crossing. The satellite has remained in this window, drifting from 1333 to 1339 LT only after other A-train missions joined the orbit; the ground track variability has generally been within 10 km over the life of the *Aqua* mission. With a swath width of approximately 2,330 km, the two instruments provide four glimpses (daytime and nighttime) of most of the earth every day. MODIS measures radiances in 36 spectral bands, including infrared and solar reflectance channels, with spatial resolution ranging from 250 m to 1 km at nadir.

The MODIS atmosphere Level-3 dataset consists of scalar statistics of various cloud properties for day (and nighttime when applicable) observations for single-day, eight-day, and calendar-month time periods. These Level-3 statistics are derived from Level-2 (pixel level) datasets and calculated on a $1° \times 1°$ resolution equal angle grid. This study will specifically explore the sensor zenith angle dependence of the cloud fraction (CF), top pressure (CTP), effective radius (r_e), and optical thickness (τ) MODIS cloud properties within the Level-3 dataset.

The Level-3 CF data are aggregated from the MODIS Cloud Mask Level-2 dataset (archived filenames designated as MOD35 and MYD35 for *Terra* and *Aqua*, respectively). The Level-3 CF statistics are determined from the number of cloud pixels in the 5×5 block of 1-km pixels. The Cloud Mask uses as many as 23 channels to determine the confidence that a given pixel is cloud free. An overview of the Cloud Mask algorithm and processing paths can be obtained from Ackerman et al. (1998) and Frey et al. (2008). The CTP is retrieved from the corresponding 5×5 block of cloudy pixels using the CO_2 slicing algorithm [Menzel et al. (2008); the CTP dataset is archived in the files designated as MOD06 and MYD06 for *Terra* and *Aqua*, respectively]. The cloud optical and microphysical properties (τ and r_e) are retrieved on a pixel-by-pixel basis using channels in the visible and shortwave-infrared, but also ingest the Cloud Mask and CTP results as part of the algorithm processing path [Platnick et al. (2003); the τ and r_e datasets are also archived in the files designated as MOD06 and MYD06 for *Terra* and *Aqua*, respectively]. Therefore, artifacts in the Cloud Mask can propagate into the τ and r_e retrievals. As mentioned above, the Level-3 statistics are calculated for the Level-2 pixels data; a full description of the Level-3 aggregation method is contained in King et al. (2003).

The viewing geometry of each Level-3 grid cell can be described by four angles: sensor zenith, solar zenith, sensor azimuth, and solar azimuth. These four angles can be used to derive the photon scattering angle between the sun and the sensor. Cloud properties derived from solar channels are dependent on the scattering angle, a component of which is the sensor zenith angle. The scattering angle (Θ) is calculated from these four angles and is defined as the angle between the photon path before and after it is scattered by the observed cloud; for MODIS it is defined by

$$\Theta = \cos\{-1[\sin(\mu_0)\sin(\theta)\cos(\phi) + \cos(\mu_0)\cos(\theta)]\}$$

where θ is the solar zenith angle, μ_0 is the sensor zenith angle, and ϕ is the azimuth angle (where ϕ is a combination of the sensor and solar azimuth angles). For this study, we will address only the relationship between the sensor zenith angle and the cloud properties, even though there are significant biases due to solar angles in the cloud optical properties.

For this study, we will primarily use the *Terra* data record, unless otherwise noted. Only small differences exist between the MODIS *Aqua* and *Terra* cloud algorithms. Global differences among the cloud datasets are small (e.g., *Aqua* CF is 2% larger than *Terra* CF), and while regional differences are larger over certain cloud regimes, as shown in Ackerman et al. (2008), the relationships between sensor zenith angle and other clouds' properties are the same for both instruments.

3. Method

The viewing geometry of any Level-3 $1° \times 1°$ grid cell, as noted above, can be described by three angles: sensor zenith, solar zenith, and relative azimuth between sensor and solar azimuths. These three angles can be used to

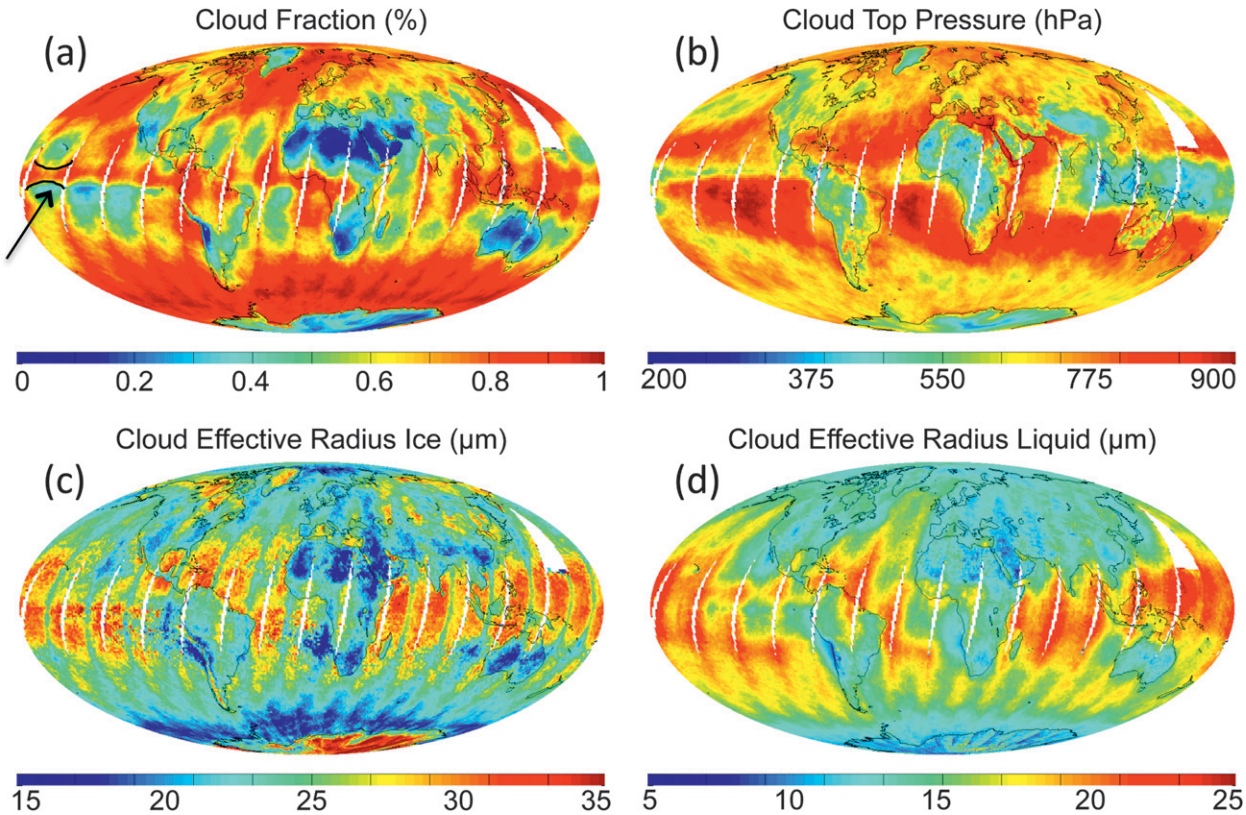

FIG. 1. The mean cloud properties for a single orbit day of MODIS *Terra* show distinct patterns that are not seen in the long-term mean. (a) Cloud fraction, (b) cloud-top pressure, (c) effective radii for ice, and (d) liquid-phase clouds are shown. Every 16th day of the MODIS time record for 2003–2007 was included in the average.

derive the photon scattering angle between the sun and the sensor. Cloud properties derived solely from the IR channels, such as the cloud-top pressure, are not directly influenced by solar angles; however, some solar channels are used in the Cloud Mask, meaning that some dependencies on solar angles may exist in the CF and propagate into the CTP and other cloud properties. Cloud properties, such as τ and r_e, derived from solar radiation are dependent on the scattering angle, a component of which is the sensor zenith angle. For this paper we will not attempt to differentiate between solar geometry dependencies and sensor zenith angle dependencies.

The *Aqua* and *Terra* satellite platforms are polar orbiting with repeating 16-day orbit precessions matching the World Reference System 2 (WRS-2) grid. Therefore, each satellite will repeat the same swath coverage every 16th day. For each day in the 16-day period the spatial coverage will contain a different set of swaths across the globe than the other 15 days of the precession. For this reason, time-averaged atmospheric products derived from MODIS are an aggregation of data obtained from a range of sensor zenith angles, from nadir to 66°. Obviously, the solar and scattering angles will also change significantly during the year within each grid cell, but we will not directly address dependences of cloud properties on the solar and scattering angles in this paper.

With the stable MODIS orbits, both temporally and geospatially, we have the unique ability to composite the long-term cloud properties derived from polar-orbiting satellite data around the sensor zenith angle. This is accomplished by averaging a single day in the orbit precession for the length of the MODIS data record. In essence, 16 geostationary records of the global cloud field for the entire period of observation and each satellite can be created, which we will refer to as an orbit day. The MODIS Level-3 dataset includes all times at which data were collected. Individual swaths begin to overlap at latitudes poleward of approximately 27° with overlap of significantly different sensor zenith angles of swaths beginning poleward of 35°. When the swaths begin to overlap, the sensor zenith angle corresponding to each grid cell on any given day may include multiple swaths and therefore multiple sensor zenith angles.

Figure 1a shows the mean daytime CF from *Terra* for every 16th day of data beginning on 1 January 2003 and ending 31 December 2008. That is, the first orbit day CF

is the mean of days 1, 17, 33, 49, etc., for the 5-yr *Terra* satellite record. This long-term averaging greatly reduces the spatial variability in the cloud data field while ensuring that only observations from a narrow band of sensor zenith angles are contained in each grid cell. Each orbit day mean contains data from 137 individual days of data, which equates to each $1° \times 1°$ grid cell containing up to 66,000 observations near the equator. Because swaths begin to overlap outside of latitudes poleward of 35° and thus varying viewing geometries are included, we will exclude all data greater than 35° from the equator for all other results; it was included in Fig. 1 to provide an example global view.

Note that the artifact in the datasets over the western Pacific (an incomplete swath on the right side of the map that falls in two different days) is contingent on how the MODIS dataset is constructed. Because MODIS has a 16-day precession and only data in which each granule (5 min of swath data) starts between 0000 and 2359 UTC is included in a given daily Level-3 data file, there is a small gap in that location. This is where data are observed but included in the proceeding or following orbit day.

4. Results

a. Orbit day composites

The spatial features across each swath of the orbit day average CF in Fig. 1a exhibit similar patterns to each other. Most notable is the U-shape feature across each swath; an example is pointed to by the arrow and lines, to the north and south of tropical deep convection and on the equatorial side of the storm belts at ±30°. This pattern, which indicates smaller CF in the center of the swath and larger at the edges, likely results from a combination of three factors: (i) the sensor zenith angle (e.g., perspective) and cloud vertical and horizontal thickness, (ii) the increase in pathlength with increase in sensor zenith angle, and (iii) the increase in pixel size with increase in sensor zenith angle.

As the sensor zenith angle becomes more oblique, the number of ''holes'' viewed between clouds decreases because more of the sides of clouds are viewed from the satellite's perspective rather than the clear region between the clouds.

Another contributing factor to the U shape in each swath involves the geometric thickness of the optically thin clouds. As the pathlength through the atmosphere between the sensor and the earth's surface increases with more oblique sensor zenith angle, there is a higher probability that a pixel accumulates enough signal from the cloud for it to be detected. The pathlength increases from nadir to the edge of scan at a rate of approximately one divided by the cosine of the sensor zenith angle.

This increase in pathlength means that a longer path through the upper troposphere will be observed at higher sensor angles than at nadir. Much of the tropics are thought to be covered by optically thin cirrus (Hong et al. 2007). Therefore, clouds with an optical thickness less than or near 0.3 that might go undetected near nadir, may be detected at higher sensor angles due to the accumulation of signal from clouds along the longer path (Ackerman et al. 2008). Thus as the cirrus shield produced by the deep convection thins with distance from the convection, the ability to detect clouds decreases along the center more quickly than near the edge of scan.

Also, at high angles the pixel size increases, creating a higher probability that at least some cloud will be seen in each pixel, thereby flagging the entire scene as cloudy (Ackerman et al. 2008). These three geometric factors work to increase the CF along the swath at higher sensor zenith angles relative to along the swath near nadir. With distance away from the deep convection we would expect a decrease in the cloud vertical thickness and horizontal extent. Obviously this will reduce the CF, resulting in a more rapid decrease in CF along nadir than along the edge of scan as the holes between clouds will be seen first near nadir because of the relatively small pixel size and pathlength.

Using the above reasoning, we would expect the greatest biases to be in regions where there are some clouds (e.g., between 20% and 80% CF) but not in regions that are predominately clear, nor in regions overcast with opaque clouds. Because relatively few holes would exist in overcast regions, such as over tropical deep convection or marine stratocumulus decks where CFs are near 100% regardless from what sensor angle the observation is made, we would expect a relatively small CF difference between nadir and edge pixels. Thus, places such as areas of small convective cloud produced by daytime heating over land or within the oceanic subtropical highs should exhibit relatively larger CF differences than the rest of the globe. We might also expect differences adjacent to regions of persistent deep convection, where large amounts of thin cirrus will exist.

The orbit day mean CTP in Fig. 1b exhibits a pattern that is similar to the CF but far less pronounced. We would expect the CTP to be larger (lower altitude) for clouds observed nearer nadir and smaller (higher altitude) nearer to the edge of scan because the pathlength of the observation is longer at the edge of scan. The longer pathlength and more oblique angle between the sensor and the earth's surface means a cloud is more likely to be seen higher in the atmosphere. A U-shaped CTP pattern can be seen in many of the same locations as in the CF field pattern; the most pronounced of which is over the Pacific Ocean near the edge of the cirrus shield

from tropical deep convection. This is most likely caused by the accumulation of cloud signal along the increased pathlength; because the cirrus clouds are optically thin we would expect that clouds near the 0.3 minimum τ−detection threshold (Ackerman et al. 2008) are missed near nadir but seen at the edge of scan.

The orbit day mean r_e for ice- and liquid-phase clouds in Figs. 1c,d, respectively, also shows significant cross swath features, where the r_e of liquid looks similar to the CF and the r_e of ice does not have readily similar spatial patterns to that seen in the CF. The r_e of ice-phase clouds has regions of relatively small size along the middle of each swath. These regions are similar to but do not correspond directly to the sunglint region and are due to dependencies on the scattering angle, which is not addressed here. The r_e of liquid-phase clouds shows a general increase in size with increasing sensor zenith angle. There are also significant differences between the adjacent regions over land and water surfaces (e.g., northern Brazil, India, Indonesia), which are also likely due to sunglint and other surface characterizations.

b. Long-term composites

The orbit day mean cloud properties in Fig. 1 demonstrate the effect sensor zenith angle has on derived cloud properties. This effect becomes less pronounced when all 16 orbit days of data are combined and long-term averages of the cloud properties are created. However, by compositing the cloud properties around various viewing geometries using all 16 days of the orbit precession we can see this effect on the long-term mean cloud fields. Figure 2 shows the 2003 to 2007 mean cloud properties for all observations near nadir (nadir to 10°) and near the edge of scan (60° and greater) from *Terra*. The number of pixels observed between nadir and 10° is approximately 8.5% of all pixels observed, and the number of pixels observed between 60° and the edge of scan is approximately 6.5% of all pixels observed.

The CF in Fig. 2a shows a marked increase everywhere except over regions with virtually no cloud, such as the Sahara Desert, or overcast, such as regions of tropical deep convection. This is intuitive because regions with broken clouds or thin clouds are where we would expect the largest differences to be evident, such as the subtropical highs and near-tropical deep convection. This has implications on the relative fraction of clouds being classified in each cloud regime. For example, higher sensor zenith angle observations will contain more trade wind cumulus than at nadir but not necessarily more tropical deep convection. This will cause a high bias in the fraction of observations classified as trade wind cumulus near the edge of scan.

The mean CTP in Fig. 2b has areas that both increase and decrease as the sensor zenith angle increases. The CTP is smaller at nadir than the edge of scan over desert and high aerosol regions (e.g., the Sahara Desert or northern India). The CTP is larger at nadir than the edge of scan over areas of land convection and oceanic broken cumulus and stratus clouds. With the exception of desert regions the CTP differences between nadir and edge of scan observations are smaller than 10 hPa (less than the expected retrieval uncertainty).

The differences in CTP between nadir and the edge of scan have implications for the classification of cloud regimes. Optically thin clouds may obscure lower clouds near the edge of scan. Clouds may also be placed higher in the atmosphere because of the inclusion of some thin high cloud into pixels containing other lower cloud types at high sensor zenith angles. Yet another implication is that high thin clouds may be included in edge of scan statistics but not included in the near-nadir statistics. For example, this would decrease the mean τ near the edge of scan relative to nadir in the long-term statistics.

The mean r_e of ice-phase clouds does not exhibit uniform increases between near nadir and near edge of scan as seen in the CF (see Fig. 2c). The differences in the mean r_e of ice clouds are only a few microns over the ocean, but some areas over land have differences of greater than 10 μm. Most of the large r_e differences occur in regions of persistent maritime stratocumulus decks, which are liquid-phase clouds. The mean r_e of liquid-phase clouds increases globally with an increase in sensor zenith angle (see Fig. 2d). This difference is greatest over areas of predominately broken clouds and where the largest differences in CF with respect to sensor zenith angle occur. Also the smallest differences are over areas with uniform cloud cover (e.g., maritime stratocumulus decks). This could indicate that increasing pixel size, and a corresponding increase in the partly cloudy field of view pixels in broken cloud regimes (e.g., trade wind cumulus), has an impact on the r_e retrieval.

The mean τ of ice clouds decreases globally with increasing sensor zenith angle (see Fig. 2e). The decrease is more significant over land, where decreases of 20 or more are observed. The mean τ of liquid clouds decreases globally, with the exception of a few locations over land in high-surface-reflectivity regions (e.g., the Sahara Desert and Himalayas), from observations taken near nadir relative to those at the edge of scan (see Fig. 2f). The largest decreases are seen over land near coastlines, like the eastern inland coastal regions of Africa, the Arabian Peninsula, and South America.

The mean of CF observations near the edge of scan (60° and greater) minus the mean near nadir (nadir to 10°) shows significant spatial variability and features. Figure 3

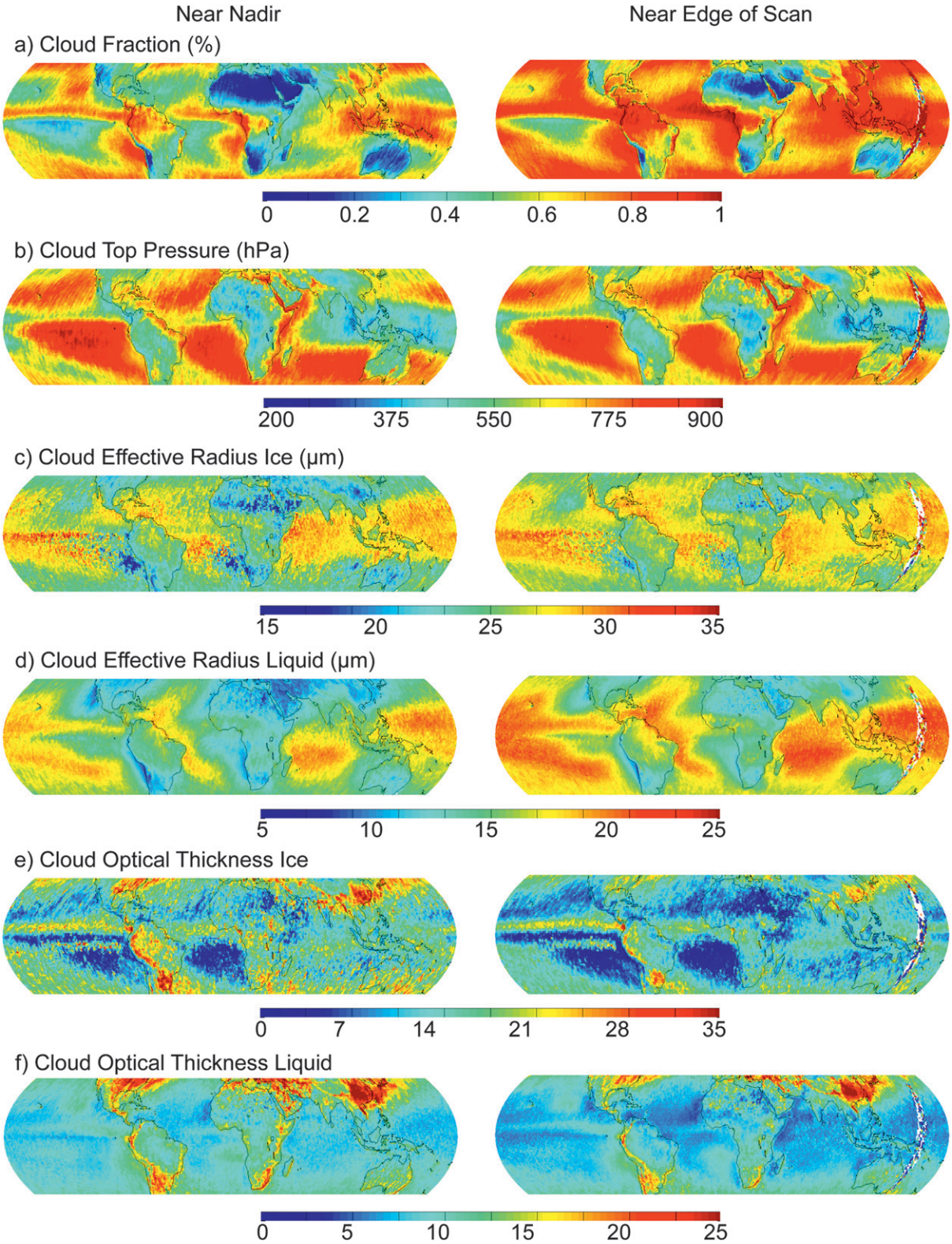

FIG. 2. The mean daytime (a) cloud fraction, (b) cloud-top pressure, (c) effective radius ice, (d) effective radius water, (e) optical thickness ice, and (f) optical thickness liquid phase are shown for 2003–2007 for observations taken from *Terra* near nadir (sensor zenith angle between nadir to 10°) and near the edge of scan (sensor zenith angle between 60° to edge of scan).

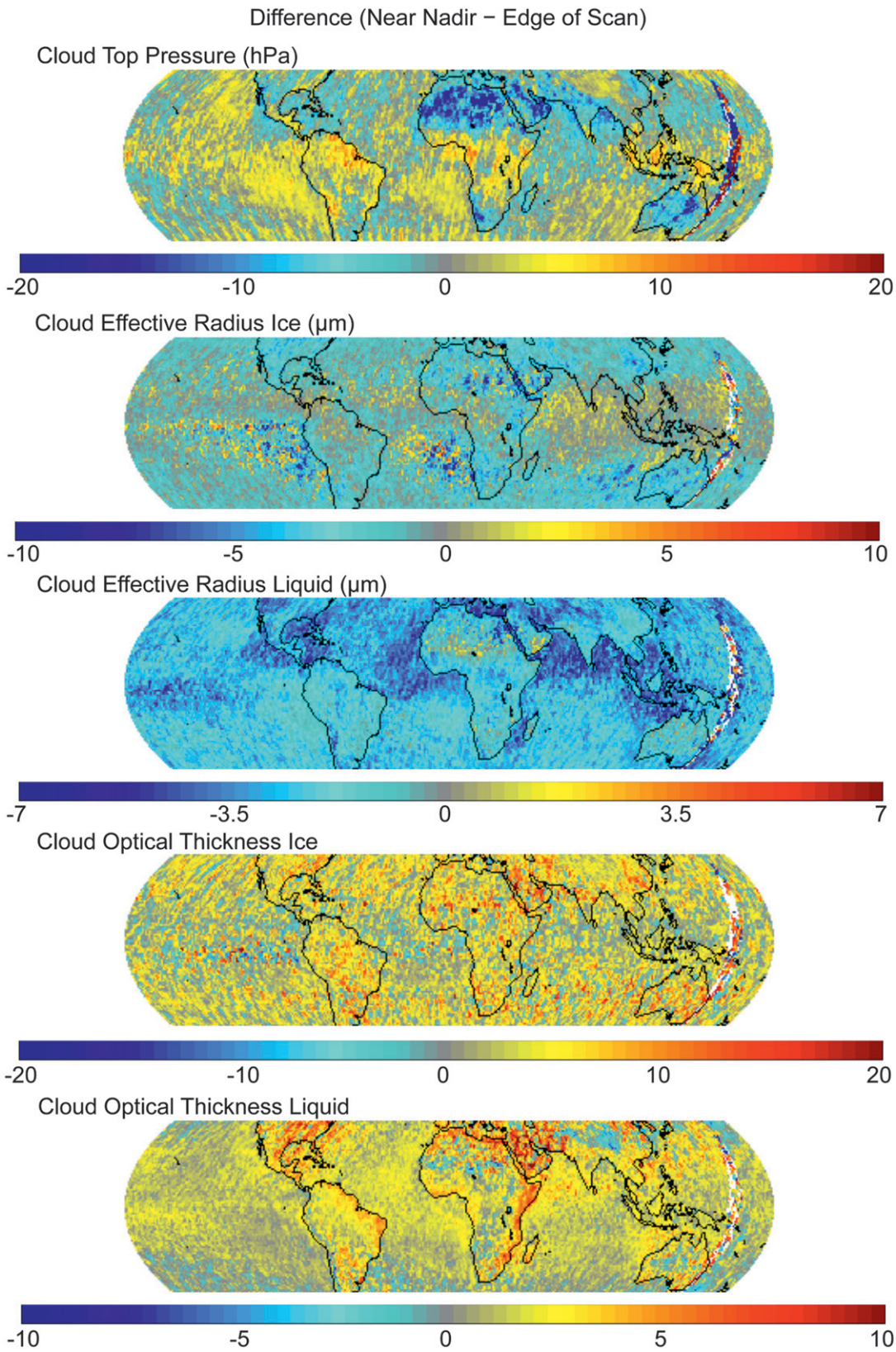

FIG. 2. (*Continued*) The difference between the (left) near nadir and (right) edge of scan is shown.

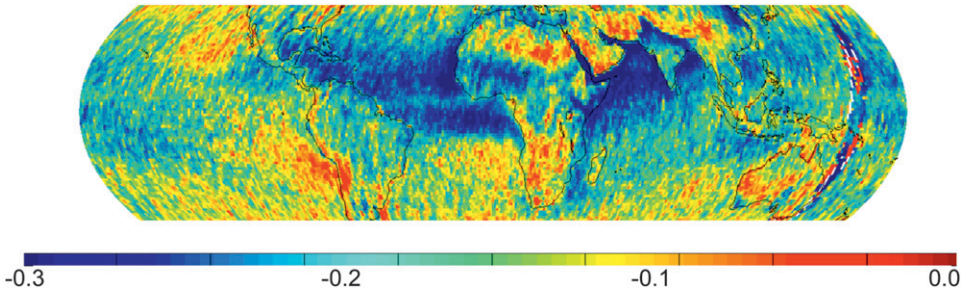

FIG. 3. The difference between the cloud fraction mean for 5 yr of *Terra* data from 2003–2007 for pixels observed for sensor zenith angles between nadir and 10° and pixels observed between 60° and the edge of scan.

shows that differences around 20% occur just north and south of the climatological mean location of oceanic tropical deep convection in the intertropical convergence zone (ITCZ), consistent with the single orbit day averages shown in Fig. 1a. Directly over the location of deep convection there is a relatively small difference, which is expected because a high CF is always observed along the ITCZ regardless of sensor zenith angle. Relative minima also occur in regions where uniform overcast cloud cover is consistently observed (e.g., the maritime stratocumulus decks, where differences range mainly between near 0 and 10%).

The most marked spatial feature in the CF difference occurs off the west coast of Africa, the northwestern Indian Ocean, and the Indian subcontinent. These maxima have a spatial pattern that is very similar to the aerosol optical thickness and mass concentration as described in Remer et al. (2006) and Remer et al. (2008). Figure 4 shows the aerosol mass concentration retrieved from *Aqua* MODIS for July 2002 through June 2006 [for a reference to this product, see Remer et al. (2006)]. There are two reasons why aerosols might be classified as cloud. First, pixels with some cloud and some aerosol are more likely to be classified as cloud than a comparable pixel without aerosol. Because pixels increase in size between nadir and edge of scan there is a higher probability that cloud and/or aerosol will be captured in a field of view. Second, at higher sensor zenith angles the path through the atmosphere seen by the satellite is longer, allowing for optically thinner aerosols and clouds to be detected. Thus, a partly cloudy pixel that also contains aerosol near the edge of scan is more likely to be classified as a cloud than an otherwise partly cloudy pixel without aerosol. This may indicate that aerosols are being classified increasingly as cloud at high sensor zenith angle. While not presented here, the aerosol products also have documented sensor zenith angle biases (Remer et al. 2006).

c. *Cloud fraction versus sensor zenith angle*

Figure 5 quantitatively shows the relationship between the mean daytime CF and sensor zenith angle. Five years of combined MODIS *Aqua* and *Terra* data were averaged in 10° sensor zenith-angle bins. The mean CF near nadir is approximately 57% and edge of scan is 71%.

This 14% increase in CF, as demonstrated in Fig. 3, is not spatially uniform. Thus it is not adequate to simply correct the global CF, regional CF, or even gridcell CF for sensor zenith angle bias using the near-nadir mean. It is important to note that the nadir view of the global CF field is not a more correct view relative to the edge-of-scan

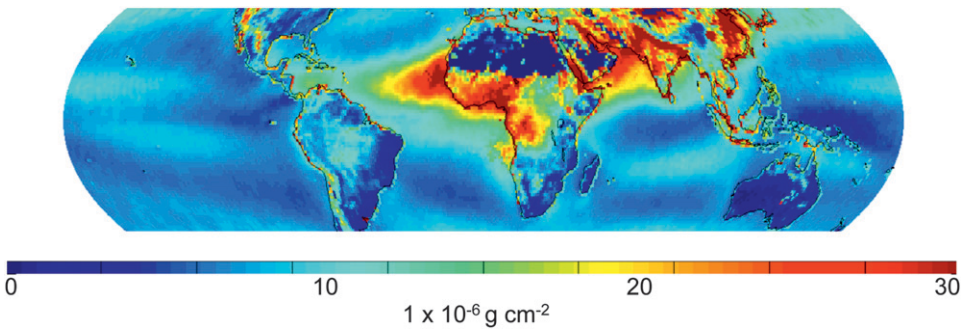

FIG. 4. Mean aerosol mass concentration showing a very similar spatial distribution to the difference in cloud fraction near nadir and edge of scan (Fig. 3).

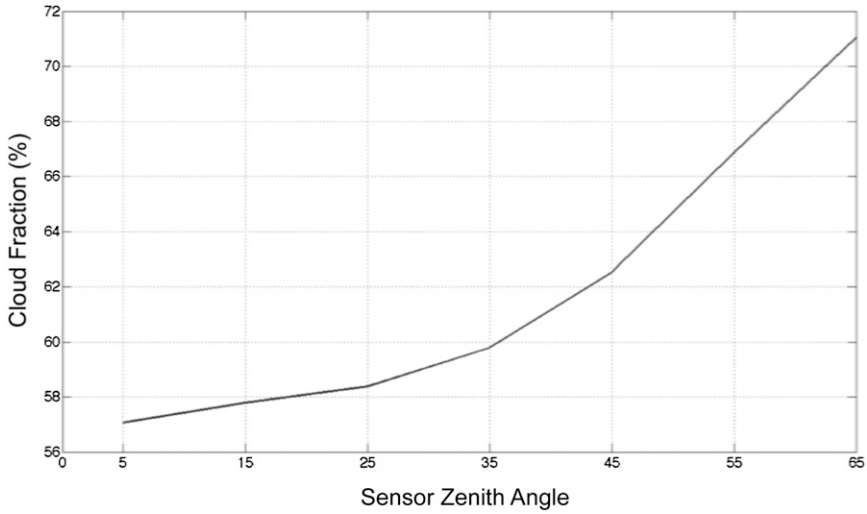

FIG. 5. The mean cloud fraction for 5 yr of combined *Aqua* and *Terra* between 35°N and 35°S latitude showing increases from 57% near nadir to over 71% near the edge of scan.

view. This is because there are large differences in the biases caused by cloud regime (e.g., it is plausible to argue that the edge-of-scan observations more accurately detect thin clouds than near nadir).

5. Conclusions and future work

Cloud coverage from satellite measurements is a function of the sensor zenith angle. All satellite data records will have these sensor zenith angle dependencies, and their impact on global cloud statistics must be considered when conducting research using cloud datasets. This paper quantifies these impacts on the MODIS cloud cover, cloud-top pressure, and cloud optical properties. The effect of sensor zenith angle on the CF is likely due to a combination of three attributes: perspective, pixel–footprint size, and increased optical pathlength through the atmosphere. While these individual effects all work to increase the CF as the sensor zenith angle increases, they likely influence the high-order cloud properties fields in different ways and not always in the same direction. The proper quantification and attribution of these effects on each cloud property requires significant further study.

As the maps in Fig. 2 clearly display, differences with the CF field and other cloud properties between observations near nadir and the edge of the swath are cloud-type dependent. Clouds such as those found in oceanic stratocumulus decks (e.g., off the coast of Peru) show little bias, but clouds that are broken or optically thin vary significantly. This is important because a satellite instrument that can easily detect small broken oceanic cumulus clouds or very optically thin clouds will be far more prone to biases from sensor zenith angle than one that cannot. Furthermore, pixels near the edge of scan are more likely to contain partly cloudy fields of view. This will negatively impact higher-order cloud properties such as r_e and τ unless accounted for.

Future research efforts will be focused on how sensor zenith angle dependencies can be accounted for when comparing MODIS with other satellite data records. Differences among various satellite platforms exist not only in the global averages but also in the regional, diurnal, and seasonal cycle averages. Also, direct pixel-level comparisons with ground-based observations would be beneficial in assessing the sensor zenith angle biases in the MODIS cloud properties. Even though angular dependencies appear to wash out in the long-term mean properties for a given geographic region, they are still present and can significantly influence comparisons between different datasets.

Acknowledgments. The authors thank the MODIS Science Team, especially Richard Frey, Michael King, and Paul Menzel. Data were acquired from the Level 1 and Atmosphere Archive and Distribution System at ladsweb.nascom.nasa.gov. Funding for this manuscript was partially provided by NASA Grants NNX08AF78A and NNX09AP02G.

REFERENCES

Ackerman, S. A., K. I. Stabala, W. P. Menzel, R. A. Frey, C. Moeller, and L. E. Gumley, 1998: Discriminating clear sky from clouds with MODIS. *J. Geophys. Res.,* **103,** 32 141–32 157.

——, R. E. Holz, R. Frey, E. W. Eloranta, B. C. Maddux, and M. J. McGill, 2008: Cloud detection with MODIS. Part II: Validation. *J. Atmos. Oceanic Technol.,* **25,** 1073–1086.

Frey, R., S. A. Ackerman, Y. Liu, K. I. Strabala, H. Zhang, J. Key, and X. Wang, 2008: Cloud detection with MODIS. Part I: Improvements in the MODIS cloud mask for Collection 5. *J. Atmos. Oceanic Technol.,* **25,** 1057–1072.

Heidinger, A. K., 2003: Rapid daytime estimation of cloud properties over a large area from radiance distributions. *J. Atmos. Oceanic Technol.,* **20,** 1237–1250.

Holz, R. E., S. A. Ackerman, F. W. Nagle, R. Frey, S. Dutcher, R. E. Kuehn, M. A. Vaughan, and B. Baum, 2008: Global Moderate Resolution Imaging Spectroradiometer (MODIS) cloud detection and height evaluation using CALIOP. *J. Geophys. Res.,* **113,** D00A19, doi:10.1029/2008JD009837.

Hong, G., P. Yang, B.-C. Gao, B. Baum, Y. X. Hu, M. D. King, and S. Platnick, 2007: High cloud properties from three years of MODIS *Terra* and *Aqua* Collection-4 data over the tropics. *J. Appl. Meteor. Climatol.,* **46,** 1840–1856.

Kahn, B. H., A. Eldering, A. J. Braverman, E. J. Fetzer, J. H. Jiang, E. Fishbein, and D. L. Wu, 2007: Toward the characterization of upper tropospheric clouds using Atmospheric Infrared Sounder and Microwave Limb Sounder observations. *J. Geophys. Res,* **112,** D05202, doi:10.1029/02006JD007336.

King, M. D., and Coauthors, 2003: Cloud and aerosol properties, precipitable water, and profiles of temperature and humidity. *IEEE Trans. Geosci. Remote Sens.,* **41,** 442–458.

Mace, G. G., Y. Zhang, S. Platnick, M. D. King, and P. Yang, 2005: Evaluation of cirrus cloud properties derived from MODIS radiances using cloud properties derived from ground-based data collected at the ARM SGP site. *J. Appl. Meteor.,* **44,** 221–240.

Mahesh, A., M. A. Gray, S. P. Palm, W. D. Hart, and J. D. Spinhirne, 2004: Passive and active detection of clouds: Comparisons between MODIS and GLAS observations. *Geophys. Res. Lett.,* **31,** L04108, doi:10.1029/2003GL018859.

Malberg, H., 1973: Comparison of mean cloud cover obtained by satellite photographs and ground-based observations over Europe and the Atlantic. *Mon. Wea. Rev.,* **101,** 893–897.

Menzel, W. P., and Coauthors, 2008: MODIS global cloud-top pressure and amount estimation: Algorithm description and results. *J. Appl. Meteor. Climatol.,* **47,** 1175–1198.

Min, Q., P. J. Minnett, and M. M. Khaiyer, 2004: Comparison of cirrus optical depths derived from GOES 8 and surface measurements. *J. Geophys. Res.,* **109,** D15207, doi:10.11029/12003JD004390.

Minnis, P., 1989: Viewing zenith angle dependence of cloudiness determined from coincident GOES East and GOES West data. *J. Geophys. Res.,* **94,** 2303–2320.

Nakajima, T., and M. King, 1990: Determination of the optical thickness and effective particle radius of clouds from reflected solar-radiation measurements. Part I: Theory. *J. Atmos. Sci.,* **47,** 1878–1893.

Naud, C., J. Muller, M. Haeffelin, Y. Morille, and A. Delaval, 2004: Assessment of MISR and MODIS cloud top heights through inter-comparison with a back-scattering lidar at SIRTA. *Geophys. Res. Lett.,* **31,** L04114, doi:10.01029/02003GL018976.

Platnick, S., and S. Twomey, 1994: Determining the susceptibility of cloud albedo to changes in droplet concentration with the advanced very high resolution radiometer. *J. Appl. Meteor.,* **33,** 334–347.

——, M. D. King, S. A. Ackerman, W. P. Menzel, B. A. Baum, J. C. Riedi, and R. A. Frey, 2003: The MODIS cloud products: Algorithms and examples from Terra. *IEEE Trans. Geosci. Remote Sens.,* **41,** 459.

Remer, L. A., D. Tanré, and Y. J. Kaufman, 2006: Algorithm for remote sensing of tropospheric aerosol from MODIS: Collection 5. [Available online at http://modis.gsfc.nasa.gov/data/atbd/atbd_mod02.pdf.]

——, and Coauthors, 2008: Global aerosol climatology from the MODIS satellite sensors. *J. Geophys. Res.,* **113,** D14S07, doi:10.1029/2007JD009661.

Rossow, W. B., 1989: Measuring cloud properties from space: A review. *J. Climate,* **2,** 201–213.

——, and R. A. Schiffer, 1999: Advances in understanding clouds from ISCCP. *Bull. Amer. Meteor. Soc.,* **80,** 2261–2287.

Smith, W. L., and C. M. R. Platt, 1978: Comparison of satellite-deduced cloud heights with indications from radiosonde and ground-based laser measurements. *J. Appl. Meteor.,* **17,** 1796–1802.

Stubenrauch, C. J., and S. Kinne, 2009: Assessment of global cloud climatologies. *GEWEX News,* No. 1, International Project Office, Silver Spring, MD 6–7.

——, A. Chèdin, G. Rädel, N. A. Scott, and S. Serrar, 2006: Cloud properties and their seasonal and dirunal variability from TOVS Path-B. *J. Climate,* **19,** 5531–5553.

Tan, B., and Coauthors, 2006: The impact of gridding artifacts on the local spatial properties of MODIS data: Implications for validation, compositing, and band-to-band registration across resolutions. *Remote Sens. Environ.,* **105,** 98–114.

Thomas, S., A. Heidinger, and M. Pavolonis, 2004: Comparison of NOAA's operational AVHRR-derived cloud amount to other satellite derived cloud climatologies. *J. Climate,* **17,** 4805–4822.

Twomey, S., and T. Cocks, 1989: Remote sensing of cloud parameters from spectra1 reflectance in the near-infrared. *Contrib. Atmos. Phys.,* **62,** 172–179.

Wylie, D. P., and W. P. Menzel, 1999: Eight years of high cloud statistics using HIRS. *J. Climate,* **12,** 170–184.

——, E. Eloranta, J. D. Spinhirne, and S. P. Palm, 2007: A comparison of cloud cover statistics from the GLAS lidar with HIRS. *J. Climate,* **20,** 4968–4981.

Zhao, G., and L. Di Girolamo, 2004: A cloud fraction versus view angle technique for automatic in-scene evaluation of the MISR cloud mask. *J. Appl. Meteor.,* **43,** 860–869.

——, and ——, 2006: Cloud fraction errors for trade wind cumuli from EOS-Terra instruments. *Geophys. Res. Lett.,* **33,** L20802, doi:10.1029/2006GL027088.